

Calculation of normal and leaky modes in planar waveguides based on a semi-analytical spectral element method

Caiwang Shi¹, Hengxin Ren¹, Zhengbo Li², and Xiaofei Chen¹

¹Southern University of Science and Technology

²Southern University of Science and Technology

November 22, 2022

Abstract

A semi-analytical spectral element method (SASEM) is proposed to solve for the normal and leaky modes of elastic waves propagating in a planar waveguide with a half-space substrate. For the SH-wave modes, the transparent boundary condition is used to model the SH wavefields in the half-space substrate. To solve for the PSV-wave normal modes on the (+, +) Riemann sheet and leaky modes on the (+, -) Riemann sheet, the elastic wavefields in the finite-thickness layers are modeled using the displacements, whereas the wavefields in the half-space are modeled using the P- and S-wave potentials. In the substrate, the transparent boundary condition is used for the shear wavefields, whereas semi-infinite elements are introduced to treat the radiative boundary condition of the P wavefields. Then, a polynomial eigenvalue problem is derived, which can be transformed into a standard linear eigenvalue problem. Solving the eigenvalue problem, we can obtain the solutions of the normal and leaky modes. Several numerical tests were performed to verify the effectiveness of SASEM, as well as to demonstrate its high accuracy. Modal analyses of the oscillations of the solved modes demonstrate that the leaky modes differ from the normal modes because of the increasing wavefields in the half-space. Moreover, the guided-P modes are confirmed to be more dependent on the P-waves, whereas the normal and organ-pipe modes are primarily determined by the S-waves. Besides the crustal model composed of several homogeneous layers, SASEM is applied to a vertically inhomogeneous offshore model to demonstrate its applicability. The good agreement between the theoretical guided-P modes and the dispersion spectra not only shows the correctness of SASEM when analyzing waveguides composed of gradient layers but also indicates the potential for constraining the P-wave velocity using the guided-P modes.

1 Calculation of normal and leaky modes in planar waveguides
2 based on a semi-analytical spectral element method

3

4 **Caiwang Shi^{1,4}, Hengxin Ren⁴, Zhengbo Li^{4,5} and Xiaofei Chen^{2,3,4}**

5 1 Department of Astronautical Science and Mechanics, Harbin Institute of Technology,

6 Harbin, 150001, China

7 2 Shenzhen Key Laboratory of Deep Offshore Oil and Gas Exploration Technology,

8 Southern University of Science and Technology, Shenzhen, 518055, China

9 3 Southern Marine Science and Engineering Guangdong Laboratory (Guangzhou),

10 Guangzhou, 511458, China

11 4 Department of Earth and Space Sciences, Southern University of Science and

12 Technology, Shenzhen, 518055, China

13 5 Academy for Advanced Interdisciplinary Studies, Southern University of Science

14 and Technology, Shenzhen, 518055, China

15 Abbreviated title: Mode calculation for planar waveguides

16 Corresponding author: Xiaofei Chen (chenxf@sustech.edu.cn)

17

18

19 **SUMMARY**

20 A semi-analytical spectral element method (SASEM) is proposed to solve for the
21 normal and leaky modes of elastic waves propagating in a planar waveguide with a
22 half-space substrate. For the SH-wave modes, the transparent boundary condition is
23 used to model the SH wavefields in the half-space substrate. To solve for the
24 PSV-wave normal modes on the $(+, +)$ Riemann sheet and leaky modes on the $(+, -)$
25 Riemann sheet, the elastic wavefields in the finite-thickness layers are modeled using
26 the displacements, whereas the wavefields in the half-space are modeled using the P-
27 and S-wave potentials. In the substrate, the transparent boundary condition is used for
28 the shear wavefields, whereas semi-infinite elements are introduced to treat the
29 radiative boundary condition of the P wavefields. Then, a polynomial eigenvalue
30 problem is derived, which can be transformed into a standard linear eigenvalue
31 problem. Solving the eigenvalue problem, we can obtain the solutions of the normal
32 and leaky modes. Several numerical tests were performed to verify the effectiveness
33 of SASEM, as well as to demonstrate its high accuracy. Modal analyses of the
34 oscillations of the solved modes demonstrate that the leaky modes differ from the
35 normal modes because of the increasing wavefields in the half-space. Moreover, the
36 guided-P modes are confirmed to be more dependent on the P-waves, whereas the
37 normal and organ-pipe modes are primarily determined by the S-waves. Besides the
38 crustal model composed of several homogeneous layers, SASEM is applied to a
39 vertically inhomogeneous offshore model to demonstrate its applicability. The good

40 agreement between the theoretical guided-P modes and the dispersion spectra not only
41 shows the correctness of SASEM when analyzing waveguides composed of gradient
42 layers but also indicates the potential for constraining the P-wave velocity using the
43 guided-P modes.

44 **Keywords**

45 Surface waves and free oscillations; Guided waves; Interface waves; Theoretical
46 seismology.

47 **1. INTRODUCTION**

48 Dispersion is a significant feature of waves propagating along a waveguide. The
49 computation of dispersion curves plays an important role in not only the forward
50 modeling of the waves in waveguides (Aki & Richards 2002) but also the inversion of
51 dispersion curves for waveguide structures (Dorman & Ewing 1962; Strobbia &
52 Cassiani 2007; Foiret et al. 2014). For problems in which horizontal variations in the
53 structures are negligible, the shallow parts of the Earth can be treated as a
54 multilayered planar waveguide composed of several finite-thickness layers and a
55 half-space substrate.

56 Both Rayleigh and Love waves are controlled by normal modes whose energy is
57 trapped in waveguides. Because of their strong energy, normal modes are of interest to
58 geophysicists and have been applied to many geophysical problems. The inversion of
59 surface-wave (including Rayleigh, Scholte, and Love wave) dispersion curves has
60 already proven an effective tool for the investigation of shallow surface and
61 lithospheric structures (Dorman & Ewing 1962; Xia et al. 1999; Kugler et al. 2007;
62 Wu et al. 2020). The calculation of the normal modes is essential for the inversion of
63 surface waves. There have been many studies focusing on the computation of normal
64 modes (Haskell 1953; Lysmer 1970; Chen 1993; Kausel, 2005). Based on the
65 propagation-matrix-type methods (Haskell 1953; Knopoff 1964; Chen 1993; Wu &
66 Chen 2016), the dispersion points are zeros of the secular function that is derived with
67 the free-surface or continuity boundary conditions. Since the normal modes are the

68 real zero points of the secular function, these modes can be determined efficiently and
69 accurately using a one-dimensional (1D) search. Leaky modes, by contrast, leak their
70 energy into the half-space and usually occur with smaller amplitudes on seismograms.
71 Leaky modes have attracted less attention in past decades because of their relatively
72 low energy compared with normal modes. We are interested in these leaky modes,
73 especially guided-P modes because they are potentially useful for the retrieval of
74 waveguide structures. Guided-P modes, which can be observed in waveguides with
75 high Poisson ratios such as the unconsolidated Earth surface and shallow marine
76 sediments (Robertsson et al. 1996; Roth et al. 1998; Boiero et al. 2013), are a part of
77 leaky modes and primarily controlled by the P-wave structures. Guided-P modes
78 provide the possibility of inverting for the P-wave structures, which is very attractive
79 because conventional inversions with normal modes can mostly image the S-wave
80 velocity structure. To investigate the inversion with leaky modes, it is essential to
81 calculate the leaky-mode dispersion curves. Although there have been some trials that
82 retrieved P-wave velocities using guided-P modes (Roth & Holliger 1999; Shtivelman
83 2004; Boiero et al. 2013; Li et al. 2018), the determination of leaky modes remains a
84 difficult task because leaky modes correspond to the complex zero points of the
85 secular functions.

86 When solving for the leaky modes, the performance of a direct search in the
87 complex domain is poor because of the huge computation involved.

88 Secular-function-based methods with iterative schemes perform much better. These
89 iterative methods first start from a series of estimations of the leaky-mode roots (these

90 estimations can be the roots of the adjoining frequency or wavenumber), and then, an
91 iterative algorithm such as the Newton–Raphson method (NRM) is applied to search
92 for the accurate roots (Gilbert 1964; Cochran et al. 1970; Radovich & De Bremaecker
93 1974; Watson 1972). The main drawback of an iterative scheme is that the estimations
94 of the roots must be sufficiently reliable; otherwise, root missing occurs. The Cauchy
95 integration method (CIM) is a more general method to search for the zeros of an
96 analytic function (Delves & Lyness 1967; Smith et al. 1992; Michalski & Mustafa
97 2018). CIM first determines the number of roots located inside the closed integral
98 path using the argument principle. The roots are then determined by solving a
99 specially constructed polynomial equation that shares the same roots as the secular
100 function. However, for an arbitrary waveguide, CIM requires reliable estimations of
101 the searching range in which the interested modes are located. It is conceivable that a
102 too-small searching range will rule out some of the modes. Meanwhile, a too-large
103 searching range not only decreases the integral accuracy but also leads to redundant
104 computation because calculating the derivatives of the secular function required in
105 CIM is cumbersome (Glytsis & Anemogiannis 2018). Moreover, CIM still suffers
106 from root missing, especially when some of the roots are located close to each other
107 (Chen et al. 2000; Glytsis & Anemogiannis 2018).

108 The secular function is usually derived on the basis of the assumption that each
109 layer of the multilayered waveguide is homogeneous. Thus, the
110 secular-function-based method is only accurate when treating layered-homogeneous
111 waveguides. To solve for the modes of more complex waveguides, discretization

112 methods, such as the finite-difference (Huang et al. 1996), pseudo-spectral (Huang
113 2006; Denolle et al. 2012), finite-element (Grant et al. 1994; Kausel 2005; Haney &
114 Tsai 2017), and spectral-element (Treyssede 2016; Hawkins 2018) methods, have
115 been applied to modal analyses. These methods discretize the waveguide into
116 numerous nodes (elements) and calculate the modes by solving a matrix eigenvalue
117 problem. Because each node has independent model parameters, these discretization
118 methods are more suitable for planar waveguides composed of inhomogeneous media.
119 The computation of these methods primarily lies in the process of eigenvalue
120 decomposition. For simplicity, a linear eigenvalue problem that is easy to solve is
121 always preferred. When solving normal modes whose eigen displacements decay
122 exponentially in the half-space substrate, the application of the truncated boundary
123 condition (Haney & Tsai 2017) or the semi-infinite element method (Valenciano &
124 Chaplain 2005; Hawkins 2018) results in simple linear eigenvalue problems. However,
125 the truncated boundary condition and the semi-infinite element method are invalid for
126 the determination of leaky modes because the eigen displacements of leaky modes are
127 nonintegrable in the half-space substrate. Extra and special treatments for the
128 wavefields in the half-space are required. The boundary element method (Mazzotti et
129 al. 2013), as well as the analytical transparent boundary condition (Uranus et al. 2004;
130 Hayashi & Inoue 2014), can exactly describe the wavefields without the discretization
131 of the half-infinite substrate. However, when applied to solid waveguides, these
132 methods result in highly nonlinear eigenvalue problems that are very difficult to solve.
133 Alternatively, the perfectly matched layer (PML) technique has been adopted in

134 several studies to simulate the half-infinite substrate (Huang et al. 1996; Treysede et
135 al. 2014) because the PML technique results in a linear eigenvalue problem. One of
136 the main drawbacks of PML is the appearance of the so-called Berenger modes that
137 only depend on the PML parameters (Zhu et al. 2010). Careful modal sifting is
138 required to filter the Berenger modes out of the modal solutions (Treysede et al.
139 2014). Additionally, the selection of the PML parameters is extremely important to
140 obtain accurate modal solutions.

141 In this paper, we propose an effective and convenient method, called the
142 semi-analytical spectral element method (SASEM), for the calculation of normal and
143 leaky modes. Instead of PML, the transparent boundary condition and semi-infinite
144 element method are adopted to exactly determine the wavefields in the half-space. For
145 SH-wave modes, SASEM results in linear eigenvalue problems with simple
146 mathematical processing. To avoid the nonlinear eigenvalue problem for PSV-wave
147 modes, we describe the wavefields in the half-space substrate with P- and S-wave
148 potentials instead of displacements and only focus on the normal modes located on the
149 $(+, +)$ Riemann sheet, as well as the leaky modes located on the $(+, -)$ Riemann sheet.
150 SASEM can simultaneously solve for the normal and leaky modes without any prior
151 information. Moreover, SASEM can conveniently handle modal problems for
152 complex planar waveguides composed of gradient layers. The dispersion curves of
153 multilayered waveguides composed of both homogeneous and gradient layers are then
154 calculated to verify the effectiveness of SASEM.

155 2. SASEM CALCULATION FOR NORMAL AND LEAKY MODES

156 The spectral element method (SEM) is widely used for the simulation of wave
 157 propagation problems (e.g., Seriani et al. 1992; Priolo et al. 1994). The main
 158 advantages of SEM are the spontaneous fulfillment of the free-surface boundary
 159 condition and high accuracy because of its high-order Gauss-type quadrature.

160 For a modal analysis of a multilayered elastic waveguide, the governing equations
 161 are expressed in the frequency–wavenumber (f – k) domain (Denolle et al. 2012;
 162 Hawkins 2018):

$$163 \quad \rho\omega^2 W(z) - k^2 \mu W(z) + \mu \frac{\partial^2 W(z)}{\partial z^2} = 0, \quad (1)$$

$$164 \quad \rho\omega^2 U_r(z) - k^2 (\lambda + 2\mu) U_r(z) - k\lambda \frac{\partial U_z(z)}{\partial z} - k \frac{\partial}{\partial z} [\mu U_z(z)] + \frac{\partial}{\partial z} \left[\mu \frac{\partial U_r(z)}{\partial z} \right] = 0, \quad (2)$$

$$165 \quad \rho\omega^2 U_z(z) - k^2 \mu U_z(z) + \mu k \frac{\partial U_r(z)}{\partial z} + k \frac{\partial}{\partial z} [\lambda U_r(z)] + \frac{\partial}{\partial z} \left[(\lambda + 2\mu) \frac{\partial U_z(z)}{\partial z} \right] = 0, \quad (3)$$

166 where $W(z)$, $U_r(z)$, and $U_z(z)$ denote the SH and PSV displacements that depend on
 167 the depth z , ρ represents the density, $\mu = \rho\beta^2$ and $\lambda = \rho\alpha^2 - 2\rho\beta^2$ represent the
 168 Lamé parameters, α is the velocity of the P-waves, β is the velocity of the S-waves,
 169 and k is the horizontal wavenumber.

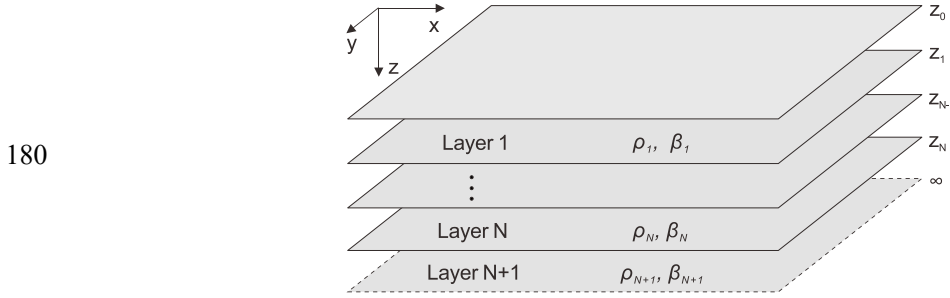
170 The dispersion curves of different modes can be determined by searching for
 171 non-trivial solutions that satisfy the source-free governing equations. With SASEM,
 172 the governing equations are discretized into a linear eigenvalue problem such that

$$173 \quad \mathbf{A}\mathbf{V} = x\mathbf{B}\mathbf{V}, \quad (4)$$

174 where x is the eigenvalue that can determine the wavenumber k . Once the complex
 175 wavenumber k is obtained, the phase velocity of this mode can be calculated using

176 $v_r = \omega/\text{Re}(k)$. Meanwhile, the attenuation of this mode is defined as $-\text{Im}(k)$. Because
 177 the wavefield solution of Eq. (4) is horizontally analytical and vertically discrete, our
 178 method is called semi-analytical SEM (i.e., SASEM).

179 2.1 SASEM for the SH-wave modes



181 Figure 1 Illustration of a multilayered planar waveguide

182

183 To introduce SASEM for the calculation of the dispersion curves, we start with the
 184 simple SH-wave case. A multilayered planer waveguide (Fig. 1) with a half-space
 185 substrate is used to simulate a shallow Earth model. We first multiply Eq. (1) by an
 186 arbitrary basis function $\varphi(z)$ and integrate over the depth range of $[z_0, z_N]$. Then, we
 187 obtain the following weak form:

$$188 \int_{z_0}^{z_N} \rho \omega^2 W \varphi dz - k^2 \int_{z_0}^{z_N} \mu W \varphi dz + \int_{z_0}^{z_N} \mu \frac{\partial^2 W}{\partial z^2} \varphi dz = 0. \quad (5)$$

189 Carrying out integration by parts on the left side of Eq. (5), we have

$$190 \int_{z_0}^{z_N} \rho \omega^2 W \varphi dz - k^2 \int_{z_0}^{z_N} \mu W \varphi dz - \int_{z_0}^{z_N} \mu \frac{\partial W}{\partial z} \frac{\partial \varphi}{\partial z} dz + [\tau_{SH} \varphi]_{z_0}^{z_N} = 0, \quad (6)$$

191 where the term $\tau_{SH}(z) = \mu \frac{\partial W(z)}{\partial z}$ is the traction and $[\tau_{SH}(z)\varphi(z)]_{z_0}^{z_N}$ depends on the
 192 boundary conditions. Because we are interested in an Earth model, the free-surface
 193 boundary condition is adopted at the top interface and, therefore, we have

$$194 \quad \tau_{SH}(z_0) = 0. \quad (7)$$

195 To mathematically describe the boundary condition at the depth z_N , we must
 196 consider the expression of the SH displacement in the half-space substrate. Because
 197 there are no upgoing waves in the substrate, the displacement in the substrate (labeled
 198 as the $[N + 1]^{\text{th}}$ layer) can be expressed as

$$199 \quad W^{(N+1)}(z) = W^{(N+1)}(z_N) e^{-i\gamma_{N+1}(z-z_N)} \quad (z \geq z_N), \quad (8)$$

200 where γ_{N+1} denotes the vertical wavenumber of the SH waves in the substrate. γ_{N+1}
 201 satisfies the following wavenumber relation:

$$202 \quad k^2 = \frac{\omega^2}{\beta_{N+1}^2} - \gamma_{N+1}^2. \quad (9)$$

203 With Eq. (8), the traction boundary condition at the depth z_N is given by

$$204 \quad \tau_{SH}(z_N) = -i\gamma_{N+1}\mu W(z_N). \quad (10)$$

205 Using Eqs. (7), (9), and (10), we can rewrite Eq. (5) as

$$206 \quad \int_{z_0}^{z_N} \left(\omega^2 \rho - \frac{\omega^2 \mu}{\beta_{N+1}^2} \right) W \varphi dz - \int_{z_0}^{z_N} \mu \frac{\partial W}{\partial z} \frac{\partial \varphi}{\partial z} dz + \gamma_{N+1}^2 \int_{z_0}^{z_N} \mu W \varphi dz - i\gamma_{N+1} \mu_{N+1} W(z) \varphi(z) \Big|_{z_N} = 0. \quad (11)$$

207 Discretization of Eq. (11) results in a quadratic eigenvalue problem in the form of

$$208 \quad \mathbf{M}^{(SH)} \mathbf{W} = \gamma_{N+1}^2 \mathbf{K}_2^{(SH)} \mathbf{W} + \gamma_{N+1} \mathbf{K}_1^{(SH)} \mathbf{W}, \quad (12)$$

209 where $\mathbf{M}^{(SH)}$, $\mathbf{K}_1^{(SH)}$, and $\mathbf{K}_2^{(SH)}$ are the coefficient matrices determined by the model
 210 parameters and \mathbf{W} contains the discrete SH displacements at different nodes.

211 Discretization methods for Eq. (12) can be either the finite element method or SEM;

212 we chose SEM in this study for its high accuracy with the usage of the Gauss–
 213 Lobatto–Legendre (GLL) quadrature.

214 Introducing a new vector $\mathbf{W}_1 = \gamma_{N+1} \mathbf{W}$, Eq. (12) can be converted into a common
 215 linear eigenvalue problem:

$$216 \quad \begin{bmatrix} \mathbf{0} & \mathbf{I} \\ \mathbf{M}^{(SH)} & -\mathbf{K}_1^{(SH)} \end{bmatrix} \begin{bmatrix} \mathbf{W} \\ \mathbf{W}_1 \end{bmatrix} = \gamma_{N+1} \begin{bmatrix} \mathbf{I} & \mathbf{0} \\ \mathbf{0} & \mathbf{K}_2^{(SH)} \end{bmatrix} \begin{bmatrix} \mathbf{W} \\ \mathbf{W}_1 \end{bmatrix}. \quad (13)$$

217 This linear eigenvalue problem can easily be solved using mathematical software
 218 and libraries. Once the eigenvalue γ_{N+1} is obtained, the horizontal wavenumber k can
 219 be determined using Eq. (9).

220 **2.2 SASEM for the PSV-wave modes**

221 The dispersion curves of the PSV waves are much more complicated than those of the
 222 SH waves because both P- and S-wave contribute to PSV dispersion. Because of the
 223 multivalued vertical wavenumbers in the half-space substrate, the modal solutions are
 224 assigned to four Riemann sheets according to the different choices of P- and S-wave
 225 vertical wavenumbers (Watson 1972). The normal modes exist on the (+, +) Riemann
 226 sheet with the P- and S-wave energies both trapped in the waveguide. By contrast, the
 227 modes on the (+, -), (-, -), and (-, +) Riemann sheets leak their energy into the
 228 half-space. Specifically, the leaky modes on the (+, -) Riemann sheet represent the
 229 modes with leaky S-wave energy and nearly trapped P-wave energy (P-wave energy is
 230 horizontally attenuated as well, but the causation is the conversion between P and S
 231 waves). For practical purposes, leaky modes on the (+, -) Riemann sheet are more
 232 important than other leaky modes because (1) the modes on the (+, -) Riemann sheet

233 are easier to extract from field seismograms and (2) the guided-P modes (or Π
 234 pseudo modes, Cochran et al. 1970) on the (+, -) Riemann sheet depend primarily on
 235 the P-wave velocities and can effectively help with the retrieval of P-wave velocity
 236 structures. In this section, we focus on the computation of the PSV normal modes on
 237 the (+, +) Riemann sheet and leaky modes on the (+, -) Riemann sheet.

238 Carrying out integration by parts on the weak form of Eqs. (2) and (3), we obtain

$$239 \int_{z_0}^{z_N} \rho \omega^2 U_r \varphi dz - k^2 \int_{z_0}^{z_N} (\lambda + 2\mu) U_r \varphi dz - k \int_{z_0}^{z_N} \left(\lambda \frac{\partial U_z}{\partial z} \varphi - \mu U_z \frac{\partial \varphi}{\partial z} \right) dz - \int_{z_0}^{z_N} \mu \frac{\partial U_r}{\partial z} \frac{\partial \varphi}{\partial z} dz + [\tau_r \varphi]_{z_0}^{z_N} = 0, \quad (14)$$

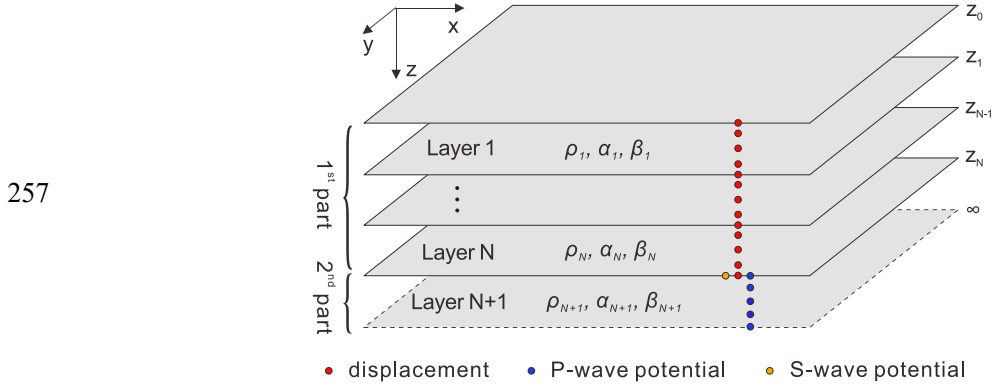
$$240 \int_{z_0}^{z_N} \rho \omega^2 U_z \varphi dz - k^2 \int_{z_0}^{z_N} \mu U_z \varphi dz + k \int_{z_0}^{z_N} \left(\mu \frac{\partial U_r}{\partial z} \varphi - \lambda U_r \frac{\partial \varphi}{\partial z} \right) dz - \int_{z_0}^{z_N} (\lambda + 2\mu) \frac{\partial U_z}{\partial z} \frac{\partial \varphi}{\partial z} dz + [\tau_z \varphi]_{z_0}^{z_N} = 0, \quad (15)$$

241 where $\tau_r(z) = \mu \frac{\partial U_r(z)}{\partial z} - k \mu U_z(z)$ and $\tau_z(z) = (\lambda + 2\mu) \frac{\partial U_z(z)}{\partial z} + k \lambda U_r(z)$ represent the
 242 tractions and $[\tau_r(z) \varphi(z)]_{z_0}^{z_N}$ and $[\tau_z(z) \varphi(z)]_{z_0}^{z_N}$ depend on the boundary conditions.

243 Different from the SH case, the tractions of the PSV waves cannot be expressed
 244 in a similar form to Eq. (10) because the displacements now contain both P and S
 245 waves. Consequently, Eqs. (14) and (15) cannot be discretized into a simple linear
 246 eigenvalue problem. However, we always prefer to obtain a linear eigenvalue problem
 247 because solving a nonlinear eigenvalue problem is very complicated and
 248 time-consuming.

249 To overcome this problem, we divide the Earth model into two parts (Fig. 2). The
 250 1st part contains the first N finite-thickness layers. In the 1st part, the PSV wavefields
 251 are described with displacements. In the 2nd part (the half-space substrate), the PSV
 252 wavefields are described using the P- and S-wave potentials. As shown in Fig. 2, the
 253 P-wave potentials in the half-space substrate are controlled using a series of discrete

254 nodes. Conversely, the S-wave potentials in the half-space substrate are determined
 255 analytically with only the S-wave potential on the interface between the Nth layer and
 256 the half-space substrate.



258 Figure 2 Illustration of the model decomposition for the PSV-wave modes

259

260 The P-wave potential (p) and S-wave potential (q) are defined as

$$261 \quad p(z) = \frac{\alpha^2}{\omega^2} \left(kU_r(z) + \frac{\partial U_z(z)}{\partial z} \right), \quad (16)$$

$$262 \quad q(z) = -\frac{\beta^2}{\omega^2} \left(kU_z(z) + \frac{\partial U_r(z)}{\partial z} \right). \quad (17)$$

263 The tractions can be expressed with the PSV potentials such that

$$264 \quad \tau_r(z) = 2k\mu \frac{\partial p(z)}{\partial z} + \mu \frac{\partial^2 q(z)}{\partial z^2} + k^2 \mu q(z), \quad (18)$$

$$265 \quad \tau_z(z) = k^2 \lambda p(z) - (\lambda + 2\mu) \frac{\partial^2 p(z)}{\partial z^2} - 2\mu k \frac{\partial q(z)}{\partial z}. \quad (19)$$

266 Additionally, the P-wave potential equation, which is the same as the acoustic

267 equation, is required to determine the P wavefields in the substrate:

$$268 \quad \rho\omega^2 p(z) - k^2 (\lambda + 2\mu) p(z) + (\lambda + 2\mu) \frac{\partial^2 p(z)}{\partial z^2} = 0. \quad (20)$$

269 Carrying out integration by parts on the weak form of Eq. (20), we obtain

$$270 \quad \int_{z_N}^{z_\infty} \rho\omega^2 p\varphi dz - k^2 \int_{z_N}^{z_\infty} (\lambda + 2\mu) p\varphi dz - \int_{z_N}^{z_\infty} (\lambda + 2\mu) \frac{\partial p}{\partial z} \frac{\partial \varphi}{\partial z} dz + \left[(\lambda + 2\mu) \frac{\partial p}{\partial z} \varphi \right]_{z_N}^{z_\infty} = 0. \quad (21)$$

271 Although the S-wave potentials in the substrate can now result in an exponential
 272 relation similar to Eq. (8), a linear eigenvalue problem is still unavailable because of
 273 the boundary conditions of the P-wave potentials in Eq. (21) and the existence of the
 274 first power term of k in Eqs. (14) and (15). To obtain a linear eigenvalue problem, the
 275 following special treatments must be applied.

276 Let $\bar{U}_z = kU_z$, $\bar{p} = kp$, and consider Eqs. (18) and (19); then, Eqs. (14), (15), and
 277 (21) can be rewritten as

$$278 \int_{z_0}^{z_N} \rho \omega^2 U_r \varphi dz - k^2 \int_{z_0}^{z_N} (\lambda + 2\mu) U_r \varphi dz - \int_{z_0}^{z_N} \left(\lambda \frac{\partial \bar{U}_z}{\partial z} \varphi - \mu \bar{U}_z \frac{\partial \varphi}{\partial z} \right) dz - \int_{z_0}^{z_N} \mu \frac{\partial U_r}{\partial z} \frac{\partial \varphi}{\partial z} dz$$

$$+ \left[\left(2\mu \frac{\partial \bar{p}}{\partial z} + \mu \frac{\partial^2 q}{\partial z^2} + k^2 \mu q \right) \varphi \right]_{z_0}^{z_N} = 0, \quad (22)$$

$$279 \int_{z_0}^{z_N} \rho \omega^2 \bar{U}_z \varphi dz - k^2 \int_{z_0}^{z_N} \mu \bar{U}_z \varphi dz + k^2 \int_{z_0}^{z_N} \left(\mu \frac{\partial U_r}{\partial z} \varphi - \lambda U_r \frac{\partial \varphi}{\partial z} \right) dz - \int_{z_0}^{z_N} (\lambda + 2\mu) \frac{\partial \bar{U}_z}{\partial z} \frac{\partial \varphi}{\partial z} dz$$

$$+ \left\{ \left[k^2 \lambda \bar{p} - (\lambda + 2\mu) \frac{\partial^2 \bar{p}}{\partial z^2} - 2\mu k^2 \frac{\partial q}{\partial z} \right] \varphi \right\}_{z_1}^{z_N} = 0, \quad (23)$$

$$280 \int_{z_N}^{z_\infty} \rho \omega^2 \bar{p} \varphi dz - k^2 \int_{z_N}^{z_\infty} (\lambda + 2\mu) \bar{p} \varphi dz - \int_{z_N}^{z_\infty} (\lambda + 2\mu) \frac{\partial \bar{p}}{\partial z} \frac{\partial \varphi}{\partial z} dz + \left[(\lambda + 2\mu) \frac{\partial \bar{p}}{\partial z} \varphi \right]_{z_N}^{z_\infty} = 0. \quad (24)$$

281 This step is used to eliminate the first power term of k in the governing equations.
 282 To simplify the boundary conditions of Eq. (24), we write the P-wave potentials in the
 283 substrate as follows, assuming that no upgoing waves exist in the substrate:

$$284 p^{(N+1)}(z) = p^{(N+1)}(z_N) e^{-iv_{N+1}(z-z_N)} \quad (z > z_N). \quad (25)$$

285 where v_{N+1} denotes the vertical wavenumber of P waves in the substrate. Accordingly,
 286 the spatial derivative of the P-wave potentials in the substrate can be expressed in a
 287 simpler form:

$$288 \frac{\partial \bar{p}^{(N+1)}(z)}{\partial z} = -iv_{N+1} \bar{p}^{(N+1)}(z) \quad (z > z_N). \quad (26)$$

289 If we are interested in the modes on the (+, +) and (+, -) Riemann sheets, the
 290 P-wave potentials will decay along the Z-direction to deeper parts and remain zero at
 291 a depth of ∞ , which satisfy the radiative boundary condition. Thus, we have the
 292 following P-wave potential boundary condition:

$$293 \quad \left. \frac{\partial \bar{p}^{(N+1)}(z)}{\partial z} \right|_{z=\infty} = 0. \quad (27)$$

294 Similarly, the S-wave potentials and spatial derivatives in the substrate have the
 295 following forms:

$$296 \quad q^{(N+1)}(z) = q^{(N+1)}(z_N) e^{-i\gamma_{N+1}(z-z_N)} \quad (z > z_N), \quad (28)$$

$$297 \quad \frac{\partial q^{(N+1)}(z)}{\partial z} = -i\gamma_{N+1} q^{(N+1)}(z) \quad (z > z_N). \quad (29)$$

298 Therefore, the terms of the S-wave potential derivatives in the boundary
 299 conditions of Eqs. (22) and (23) can be expressed analytically using Eq. (29).

300 The boundary condition terms of Eqs. (22) and (23) describe the contribution of
 301 the P- and S-wave potentials in the substrate to the displacements in the 1st part of the
 302 waveguide. The remaining task is to express the boundary conditions of the P- and
 303 S-wave potentials at the depth z_N , which describes the contribution from the
 304 displacement wavefields in the 1st part. Because no weak form of the S-wave potential
 305 equation is used, we can express the boundary conditions of the P- and S-wave
 306 potentials at the depth z_N using the Dirichlet boundary conditions:

$$307 \quad \bar{p}^{(N+1)}(z_N) = \frac{\alpha_{N+1}^2}{\omega^2} \left(k^2 U_r^{(N+1)}(z_N) + \left. \frac{\partial \bar{U}_z^{(N+1)}(z)}{\partial z} \right|_{z=z_N} \right), \quad (30)$$

$$308 \quad q^{(N+1)}(z_N) = -\frac{\beta_{N+1}^2}{\omega^2} \left(\bar{U}_z^{(N+1)}(z_N) + \left. \frac{\partial U_r^{(N+1)}(z)}{\partial z} \right|_{z=z_N} \right). \quad (31)$$

309 Considering the continuity of the displacements and the tractions at the inner

310 interfaces, the potentials at the depth z_N can be determined by the displacements

311 using

$$312 \quad \bar{p}_{N+1}(z_N) = \frac{1}{\rho_{N+1}\omega^2} \left[(\lambda_N + 2\mu_N) \frac{\partial \bar{U}_z^{(N)}(z)}{\partial z} \Big|_{z=z_N} + k^2 \lambda_N U_r^{(N)}(z_N) \right] + \frac{2k^2 \mu_{N+1} U_r^{(N)}(z_N)}{\rho_{N+1}\omega^2}, \quad (32)$$

$$313 \quad q_{N+1}(z_N) = \frac{-1}{\rho_{N+1}\omega^2} \left[\mu_N \frac{\partial U_r^{(N)}(z)}{\partial z} \Big|_{z=z_N} - \mu_N \bar{U}_z^{(N)}(z_N) \right] - \frac{2\mu_{N+1} \bar{U}_z^{(N)}(z_N)}{\rho_{N+1}\omega^2}. \quad (33)$$

314 Thus far, all the governing equations and boundary conditions of the

315 displacements and potential wavefields have been expressed explicitly. To solve for

316 the modes, we replace the term k^2 in Eqs. (22)–(24) and (32) with $\frac{\omega^2}{\beta_{N+1}^2} - \gamma_{N+1}^2$. In

317 combination with the boundary condition of Eq. (33), we obtain the final eigenvalue

318 system, which can be written as

$$319 \quad \int_{z_0}^{z_N} \left(\rho\omega^2 - \frac{\omega^2(\lambda + 2\mu)}{\beta_{N+1}^2} \right) U_r \varphi dz + \gamma_{N+1}^2 \int_{z_0}^{z_N} (\lambda + 2\mu) U_r \varphi dz - \int_{z_0}^{z_N} \left(\lambda \frac{\partial \bar{U}_z}{\partial z} \varphi - \mu \bar{U}_z \frac{\partial \varphi}{\partial z} \right) dz$$

$$- \int_{z_0}^{z_N} \mu \frac{\partial U_r}{\partial z} \frac{\partial \varphi}{\partial z} dz + \left[2\mu_{N+1} \frac{\partial \bar{p}^{(N+1)}(z)}{\partial z} - 2\gamma_{N+1}^2 \mu_{N+1} q^{(N+1)}(z) + \frac{\omega^2 \mu_{N+1}}{\beta_{N+1}^2} q^{(N+1)}(z) \right] \varphi(z) \Big|_{z=z_N} = 0, \quad (34)$$

$$320 \quad \int_{z_0}^{z_N} \left(\rho\omega^2 - \frac{\omega^2 \mu}{\beta_{N+1}^2} \right) \bar{U}_z \varphi dz + \gamma_{N+1}^2 \int_{z_0}^{z_N} \left(\mu \bar{U}_z \varphi - \mu \frac{\partial U_r}{\partial z} \varphi + \lambda U_r \frac{\partial \varphi}{\partial z} \right) dz$$

$$+ \frac{\omega^2}{\beta_{N+1}^2} \int_{z_0}^{z_N} \left(\mu \frac{\partial U_r}{\partial z} \varphi - \lambda U_r \frac{\partial \varphi}{\partial z} \right) dz - \int_{z_0}^{z_N} (\lambda + 2\mu) \frac{\partial \bar{U}_z}{\partial z} \frac{\partial \varphi}{\partial z} dz$$

$$+ \left[\left(\frac{\omega^2}{\beta_{N+1}^2} - \gamma_{N+1}^2 \right) \lambda_{N+1} \bar{p}^{(N+1)}(z) - (\lambda_{N+1} + 2\mu_{N+1}) \frac{\partial^2 \bar{p}^{(N+1)}(z)}{\partial z^2} \right] \varphi(z) \Big|_{z=z_N} = 0$$

$$+ \left[2i\omega^2 \rho_{N+1} \gamma_{N+1} q^{(N+1)}(z) - 2i\mu_{N+1} \gamma_{N+1}^3 q^{(N+1)}(z) \right] \varphi(z) \Big|_{z=z_N} = 0, \quad (35)$$

$$321 \quad \int_{z_N}^{z_\infty} \left(\rho\omega^2 - \frac{\omega^2(\lambda + 2\mu)}{\beta_{N+1}^2} \right) \bar{p} \varphi dz + \gamma_{N+1}^2 \int_{z_N}^{z_\infty} (\lambda + 2\mu) \bar{p} \varphi dz - \int_{z_N}^{z_\infty} (\lambda + 2\mu) \frac{\partial \bar{p}}{\partial z} \frac{\partial \varphi}{\partial z} dz = 0, \quad (36)$$

$$322 \quad \rho_{N+1} \omega^2 \bar{p}^{(N+1)}(z_N) = (\lambda_N + 2\mu_N) \frac{\partial \bar{U}_z^{(N)}(z)}{\partial z} \Big|_{z=z_N} + (\lambda_N + 2\mu_{N+1}) \left(\frac{\omega^2}{\beta_{N+1}^2} - \gamma_{N+1}^2 \right) U_r^{(N)}(z_N), \quad (37)$$

323
$$\rho_{N+1}\omega^2 q^{(N+1)}(z_N) = - \left[\mu_N \frac{\partial U_r^{(N)}(z)}{\partial z} \Big|_{z=z_N} - \mu_N \bar{U}_z^{(N)}(z_N) \right] - 2\mu_{N+1} \bar{U}_z^{(N)}(z_N). \quad (38)$$

324 Because of the simultaneous existence of the terms γ_{N+1} , γ_{N+1}^2 , and γ_{N+1}^3 , the
 325 discretization of Eqs. (34)–(38) results in a cubic eigenvalue problem:

326
$$\mathbf{M}\mathbf{U} = \gamma_{N+1}^3 \mathbf{K}_3 \mathbf{U} + \gamma_{N+1}^2 \mathbf{K}_2 \mathbf{U} + \gamma_{N+1} \mathbf{K}_1 \mathbf{U}, \quad (39)$$

327 where \mathbf{M} , \mathbf{K}_1 , \mathbf{K}_2 , and \mathbf{K}_3 are the coefficient matrices determined by the model
 328 parameters and \mathbf{U} is an eigenvector composed of the displacements in the
 329 finite-thickness layers and the wave potentials in the half-space substrate.

330 To solve for the eigenvalues of Eq. (39), we introduce two new temporary vectors
 331 $\mathbf{U}_1 = \gamma_{N+1} \mathbf{U}$ and $\mathbf{U}_2 = \gamma_{N+1}^2 \mathbf{U}$; then, we can convert Eq. (39) into a linear eigenvalue
 332 problem:

333
$$\underbrace{\begin{bmatrix} 0 & 0 & \mathbf{I} \\ 0 & \mathbf{I} & 0 \\ \mathbf{M} & -\mathbf{K}_1 & -\mathbf{K}_2 \end{bmatrix}}_{\mathbf{A}} \begin{bmatrix} \mathbf{U} \\ \mathbf{U}_1 \\ \mathbf{U}_2 \end{bmatrix} = \gamma_{N+1} \underbrace{\begin{bmatrix} 0 & \mathbf{I} & 0 \\ \mathbf{I} & 0 & 0 \\ 0 & 0 & \mathbf{K}_3 \end{bmatrix}}_{\mathbf{B}} \begin{bmatrix} \mathbf{U} \\ \mathbf{U}_1 \\ \mathbf{U}_2 \end{bmatrix}. \quad (40)$$

334 Because the global matrix \mathbf{B} is singular, we can compute the wavenumber using a
 335 modified form of the eigenvalue problem (Eq. (40)):

336
$$\begin{bmatrix} 0 & 0 & \mathbf{I} \\ 0 & \mathbf{I} & 0 \\ \mathbf{M} & -\mathbf{K}_1 & -\mathbf{K}_2 \end{bmatrix}^{-1} \begin{bmatrix} 0 & \mathbf{I} & 0 \\ \mathbf{I} & 0 & 0 \\ 0 & 0 & \mathbf{K}_3 \end{bmatrix} \begin{bmatrix} \mathbf{U} \\ \mathbf{U}_1 \\ \mathbf{U}_2 \end{bmatrix} = \frac{1}{\gamma_{N+1}} \begin{bmatrix} \mathbf{U} \\ \mathbf{U}_1 \\ \mathbf{U}_2 \end{bmatrix}, \quad (41)$$

337 where the eigenvalue is $\frac{1}{\gamma_{N+1}}$. Then, the horizontal wavenumber k can be obtained via
 338 simple calculations.

339 3. MODEL DISCRETIZATION

340 In SASEM, each layer with finite thickness is divided into several elements controlled
341 by GLL nodes. Using the advantages of the GLL nodes, the integrals in Eqs. (34)–(38)
342 can be easily calculated because the GLL quadrature formula converts the integral
343 into a weighted summation of the integrand functions at the GLL nodes. Additionally,
344 the spatial derivatives of the displacement (potential) functions can be efficiently
345 calculated via simple summations as well.

346 The strategy of element partition in SASEM is flexible, and we can divide each
347 layer into an arbitrary number of elements. Usually, we can assign fewer elements for
348 layers with smaller thicknesses and more elements for layers with larger thicknesses.
349 The only requirement is that the node distribution is sufficiently dense so that no
350 numerical dispersion caused by the discrete nodes affects the results. Typically, the
351 number of GLL nodes that control each element, which is denoted by N_{gll} , is
352 stationary throughout the entire model, whereas the number of GLL elements
353 (elements controlled by GLL nodes) is freely varying according to the waveguide
354 parameters and the frequencies. In our implementation, the number of GLL elements
355 (ne) in each layer is determined by the following criterion:

$$356 \quad ne_i \geq \lceil h_i / \lambda_s^{(i)} \rceil, \quad (42)$$

357 where h_i and $\lambda_s^{(i)}$ are the thickness and shear wavelength of the i^{th} layer, respectively,
358 and $\lceil \cdot \rceil$ is the rounding up function. The criterion of Eq. (42) guarantees that there
359 are at least N_{gll} nodes in each shear wavelength. To suppress the dispersion caused by

360 discrete nodes, Haney & Tsai (2017) suggested that there should be at least 5 finite
361 elements in each wavelength. Based on their schemes, we always set N_{gll} to greater
362 than 7 to achieve sufficiently high accuracy. Additionally, Eq. (42) indicates that ne
363 can be changed according to the different wavelengths (or frequencies). To achieve
364 high computation efficiency, the elements of SASEM are redivided automatically for
365 each new frequency and consequently fewer elements are used when solving for the
366 modes at low frequencies (large wavelength), which is different from Haney & Tsai
367 (2017).

368 For the half-space substrate, the improper integral in the half-infinite domain
369 $[z_N, +\infty)$ is required in Eq. (36). Because we are interested in the modes on the $(+, +)$
370 and $(+, -)$ Riemann sheets, the P-wave potentials will decay exponentially in the
371 substrate, which coincides with the displacements of the normal modes. An
372 appropriate candidate to describe these decayed P-wave potential wavefields is the
373 semi-infinite element controlled by the Gauss–Radau–Laguerre (GRL) nodes
374 (Valenciano & Chaplain 2005). Appendix A provides the details of the GRL nodes. In
375 the implementation of the semi-infinite element, besides the number of GRL nodes
376 (denoted by N_{grl}), a scale factor between the element scale and the physical scale is
377 necessary. An appropriate semi-infinite element should have (1) sufficiently dense
378 GRL nodes to sample the decaying wavefields and (2) a suitable scale factor that
379 guarantees sufficient wavefield decay at the last GRL nodes to enable the GRL
380 quadrature to be accurate. We always let the number of GRL nodes in the
381 semi-infinite element be greater than 10, and the scale factor is determined by

382
$$\eta = 5\lambda_p^{(N+1)} / \xi_{\max}, \quad (43)$$

383 where ξ_{\max} denotes the maximum coordinate of the original GRL nodes and $\lambda_p^{(N+1)}$ is
 384 the P wavelength of the half-space substrate. The criterion of Eq. (43) determines a
 385 moderate semi-infinite element in which the P-wave potentials sufficiently decay and
 386 the improper integral of Eq. (36) can be accurate.

387 4. NUMERICAL RESULTS

388 4.1 Multilayered crustal model

389 We tested our algorithm using a multilayered waveguide composed of several
 390 homogeneous solid layers. This type of model is the most discussed in common
 391 studies of surface waves. In this section, normal and leaky modes of the modified
 392 version of the CIT 11 GB model (Julian & Anderson 1968; Wu & Chen 2016) in Table
 393 1 are analyzed. The frequency range we focus on is from 0.001 to 0.05 Hz and the
 394 frequency interval is 2.5×10^{-4} Hz.

395 Table 1 Modified CIT 11 GB model

Layer no.	α [km·s ⁻¹]	β [km·s ⁻¹]	ρ [g·cm ⁻³]	h [km]
1	6.58	3.55	2.9	35
2	8.05	4.6	3.5	34
3	7.75	4.31	3.47	54
4	8.19	4.55	3.6	225
5	8.84	4.92	3.8	102
6	9.82	5.4	3.95	203
7	10.6	5.8	4.15	∞

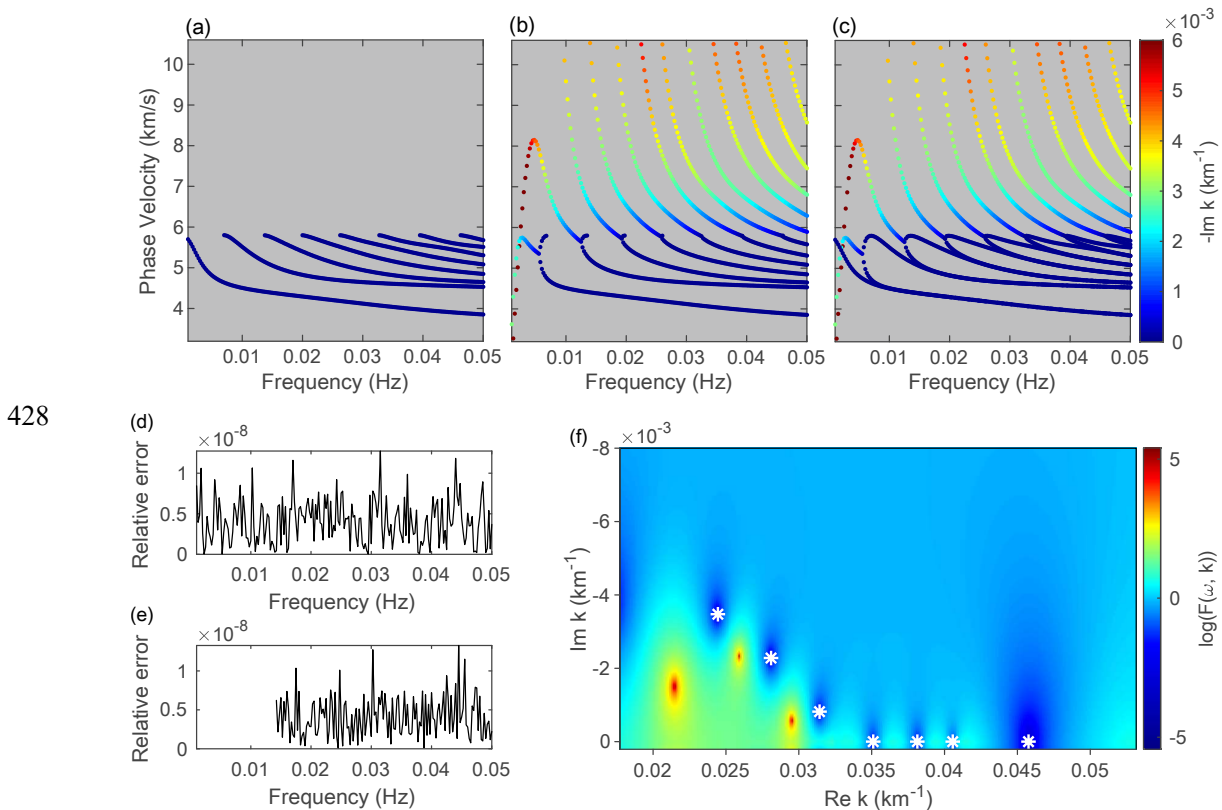
396 4.1.1 SH-wave modes

397 We first calculated the SH normal and leaky modes. When an arbitrary frequency was
398 given, the waveguide was discretized by 8-order GLL elements (controlled by 9 GLL
399 nodes). The model discretization criterion (Eq. (42)) guaranteed that there were at
400 least 9 nodes inside each wavelength. After assembling the global matrices in Eq. (11),
401 we obtained vertical wavenumbers in the substrate (γ_{N+1}), as well as the horizontal
402 wavenumbers (k). With the sign of $\text{Im}(\gamma_{N+1})$, we distinguished the normal (Fig. 3a)
403 and leaky (Fig. 3b) modes. The different colors of the modes represent the attenuation
404 factors determined by $-\text{Im}(k)$. Fig. 3c shows the combination of the normal and
405 leaky modes. To solve for the modes of all the 197 discrete frequencies, our method
406 cost 2.8 seconds on Intel(R) Core(TM) i7-7700K processor.

407 To verify the correctness of the normal modes in Fig. 3a, we calculated the errors
408 between the SASEM solutions and those given by the generalized
409 reflection/transmission coefficients method (i.e., GRTM; Chen 1993; Wu & Chen
410 2016). Assuming the GRTM solutions (wavenumber k_{GRTM}) were accurate, the
411 relative errors of the SASEM solutions were defined as $\varepsilon = |k_{SASEM} - k_{GRTM}| / |k_{GRTM}|$. As
412 can be seen in Fig. 3d and Fig. 3e, the relative errors of the fundamental and second
413 higher modes are on the order of 10^{-8} , which confirms the correctness and accuracy of
414 SASEM. To assess the correctness of the leaky SH-wave modes, we used an intuitive
415 method on the basis of the values of the secular function. Here, we take the frequency
416 of 0.03 Hz as an example. We scanned numerous complex k over a given range and
417 calculated the corresponding secular function values, as shown in Fig. 3f. A series of

418 local minima (the dark blue areas in Fig. 3f) exist in the given wavenumber range,
 419 which indicates the locations of the zero points of the secular function. In Fig. 3f,
 420 SASEM solutions (white stars) perfectly match the zero points of the secular function.
 421 Additionally, Fig. 3f indicates that no root missing occurs in the given wavenumber
 422 range.

423 Using the secular function image in Fig. 3f, the complex roots of 0.03 Hz can be
 424 roughly estimated. On the basis of these estimated roots and the GRTM-based secular
 425 function $F(\omega, k)$, NRM was then used to obtain the accurate roots (Wu & Chen 2017).
 426 For comparison, Table 2 gives the modal solutions of both SASEM and NRM. The
 427 results show the high accuracy of the SASEM solutions.



429 Figure 3 SH modal solutions and the verification: (a) normal modes; (b) leaky modes;
 430 (c) the combination of the normal and leaky modes; relative errors between the

431 SASEM solutions and GRTM solutions for the (d) fundamental mode and (e) the
 432 second higher normal mode; and (f) the agreement of the calculated leaky modes
 433 (white stars) with the secular function at 0.03 Hz.

434

435 Table 2 SH leaky-mode solutions of the SASEM and NRM at 0.03 Hz

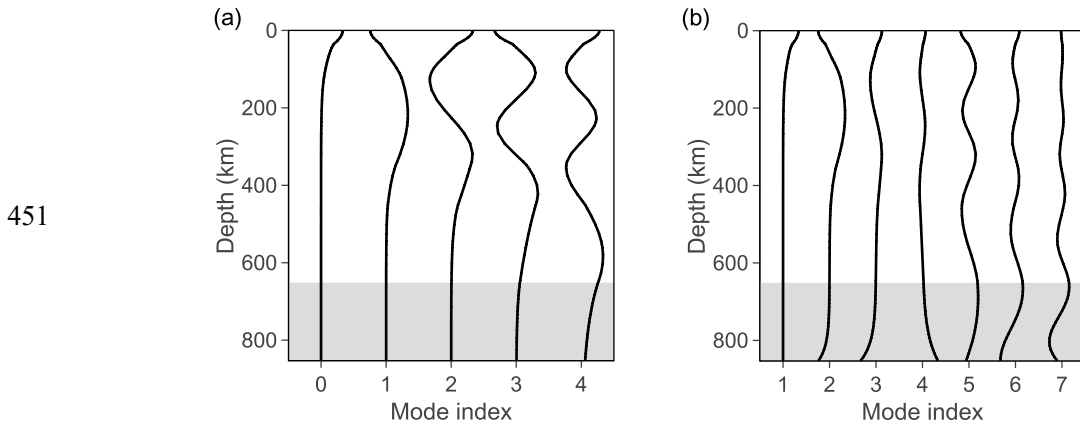
Mode	SASEM		NRM	
	$\text{Re}(k) [\times 10^{-2} \text{ km}^{-1}]$	$-\text{Im}(k) [\times 10^{-2} \text{ km}^{-1}]$	$\text{Re}(k) [\times 10^{-2} \text{ km}^{-1}]$	$-\text{Im}(k) [\times 10^{-2} \text{ km}^{-1}]$
1	4.5760984	0	4.5760984	0
2	4.0563611	0	4.0563611	0
3	3.8133166	0	3.8133166	0
4	3.5107371	0	3.5107371	0
5	3.1423246	0.0817456	3.1423246	0.0817456
6	2.8095646	0.2278961	2.8095646	0.2278961
7	2.4445172	0.3472734	2.4445172	0.3472734

436

437 For the SH-wave modes, normal modes and leaky modes convert into each other
 438 at the phase velocity that equals the half-space S-wave velocity. Below the half-space
 439 S-wave velocity, normal modes and leaky modes tend to overlap when the frequency
 440 increases. Above the half-space S-wave velocity, only the leaky modes exist and the
 441 dispersion curves of the leaky modes in this range are usually steep.

442 Because the displacements are parts of the eigenvector, we can conveniently
 443 obtain the real and imaginary parts of the corresponding SH displacements (Fig. 4)
 444 after the eigenvalue decomposition. At 0.03 Hz, there are five normal modes. Similar
 445 to the results in prior studies (e.g., Chen 1993; Wu & Chen 2016), the displacements

446 of normal modes decay rapidly in the half-space substrate (Fig. 4a). Meanwhile, there
 447 are seven leaky modes (satisfying $\text{Re}(k) \geq 0$, $\text{Im}(k) \leq 0$, and $\text{Im}(\gamma_{N+1}) > 0$) at 0.03 Hz
 448 if we filter out the modes with phase velocities greater than 10.6 km/s. The
 449 displacements of the leaky modes differ significantly from those of the normal modes
 450 because they increase in the substrate.



452 Figure 4 Displacements of the SH-wave modes at 0.03 Hz: (a) normal modes and (b)
 453 leaky modes. Only the real parts of the displacements are shown. The curves in the
 454 gray regions represent the SH displacements in the half-space.

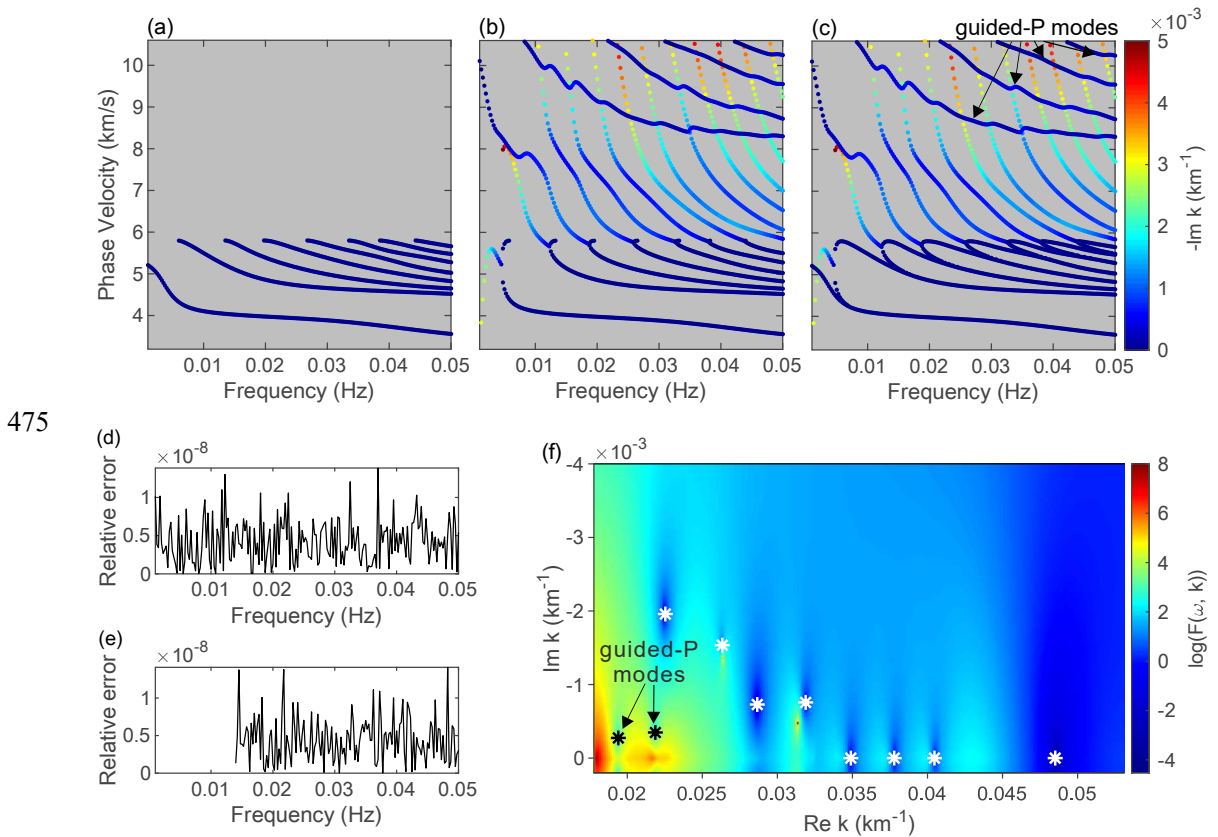
455

456 4.1.2 PSV-wave modes

457 Next, we calculated the PSV normal modes and the leaky modes on the (+, -)
 458 Riemann sheet. Because PSV wavefields are much more complicated than SH
 459 wavefields, we discretized the waveguide using several 11-order GLL elements and
 460 one 20-order GRL element. The model discretization criterion, Eq. (42), guaranteed
 461 that there were at least 12 nodes inside each wavelength. Using the eigenvalue system
 462 of Eqs. (34)–(38), we obtained a linear eigenvalue problem in the form of Eq. (41)

463 after discretization and matrix assembling. Similar to the SH case, we distinguished
 464 the normal (Fig. 5a) and leaky (Fig. 5b) modes on the basis of the sign of $\text{Im}(\gamma_{N+1})$.
 465 Based on the Intel(R) Core(TM) i7-7700K processor, the time consumed for
 466 calculating the normal and leaky modes at 197 discrete frequencies (Fig. 5c) was 18.6
 467 seconds.

468 The SASEM modal solutions can also be assessed using the GRTM solutions. In
 469 Fig. 5d and 5e, the relative errors of the fundamental and second higher modes are on
 470 the order of 10^{-8} , which confirms the correctness of SASEM for the PSV normal
 471 modes. In Fig. 5f, the leaky modes calculated using SASEM perfectly match the zero
 472 points of the secular function. The accurate roots found by NRM were also compared
 473 with the SASEM solutions. Results in Table 3 confirm the high accuracy of SASEM
 474 for the PSV leaky modes.



476 Figure 5 PSV modal solutions and the verification: (a) normal modes; (b) leaky modes
477 on the (+, -) Riemann sheet; (c) the combination of the normal and leaky modes;
478 relative errors between the SASEM solutions and GRTM solutions of the (d)
479 fundamental mode and (e) the second higher normal mode; and (f) the agreement of
480 the calculated leaky modes (stars) with the secular function at 0.03 Hz. In panel (f),
481 the two black stars represent the guided-P modes and the residual white stars represent
482 the other leaky modes.

483

484 Table 3 PSV leaky-mode solutions of SASEM and NRM at 0.03 Hz

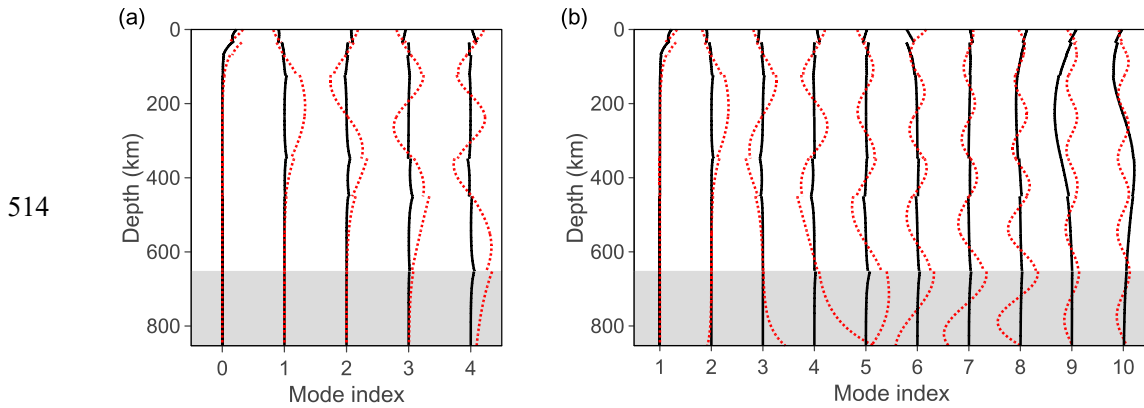
Mode	SASEM		NRM	
	$\text{Re}(k) [\times 10^{-2} \text{ km}^{-1}]$	$-\text{Im}(k) [\times 10^{-2} \text{ km}^{-1}]$	$\text{Re}(k) [\times 10^{-2} \text{ km}^{-1}]$	$-\text{Im}(k) [\times 10^{-2} \text{ km}^{-1}]$
1	4.8508702	0	4.8508702	0
2	4.0464635	0	4.0464635	0
3	3.7785823	0	3.7785823	0
4	3.4893774	0	3.4893774	0
5	3.1882687	0.0754322	3.1882687	0.0754322
6	2.8660226	0.0728643	2.8660226	0.0728643
7	2.6331815	0.1534412	2.6331815	0.1534412
8	2.2537158	0.1956290	2.2537158	0.1956290
9	2.1874208	0.0348445	2.1874208	0.0348445
10	1.9406896	0.0274573	1.9406896	0.0274573

485

486 For the PSV-wave modes, the normal and leaky modes convert into each other at
487 the phase velocity equaling the half-space S-wave velocity. The leaky PSV-wave
488 modes differ significantly from the leaky SH-wave modes in the high-phase-velocity

489 areas. Besides the strong-attenuated modes with steep dispersion curves and phase
490 velocities greater than the half-space S-wave velocity (also called organ-pipe modes),
491 some dispersion curves have weak attenuation and behave similarly to the higher
492 normal modes (Fig. 5c). This type of dispersion curve, called guided-P mode (Boiero
493 et al. 2013) or Π pseudo mode (Cochran et al. 1970), has been reported to be
494 primarily controlled by P-wave velocity structures (Li et al. 2018; Li & Chen 2020).
495 In the case of high Poisson ratios, the dispersion curves of guided-P modes are close
496 to those of pure acoustic waves (Sun et al. 2021). To study the oscillation features of
497 the calculated modes, the P- and S-wave potentials of the modes at 0.03 Hz were
498 calculated instead of the displacements because the PSV displacements consist of both
499 P and S waves (Fig. 6). The oscillation features of the normal modes (Fig. 6a) agree
500 with the conclusions of former studies in that the wavefields decay in the half-space
501 and the energy of the higher modes focuses more in deep regions. In Fig. 6b, the leaky
502 modes are numbered according to their phase velocity. Of the leaky modes studied,
503 modes 9 and 10 are guided-P modes. All the leaky modes have increasing S-wave
504 potentials and decaying P-wave potentials in the half-space, which is consistent with
505 the definition of the leaky modes on the (+, -) Riemann sheet. Differences occur
506 when we compare the relative magnitudes of the P- and S-wave potentials. For the
507 guided-P modes (modes 9 and 10 in Fig. 6b), the P-wave potentials above the
508 half-space are notably larger than the S-wave potentials, which confirms that P-waves
509 contribute more to the guided-P modes. Because of their smaller attenuation factor,
510 the guided-P modes are easier to identify than the organ-pipe modes in dispersion

511 analyses of field seismograms. With accurate calculations, guided-P-mode dispersion
512 curves have the potential to constrain P-wave velocity structures in dispersion
513 inversions.



515 Figure 6 P- and S-wave potentials of the PSV (a) normal and (b) leaky modes at 0.03
516 Hz. The black solid lines represent the P-wave potentials, and the red dotted lines
517 represent the S-wave potentials. Only the real parts of the potentials are shown. The
518 curves in the gray regions represent the P- and S-wave potentials in the half-space.

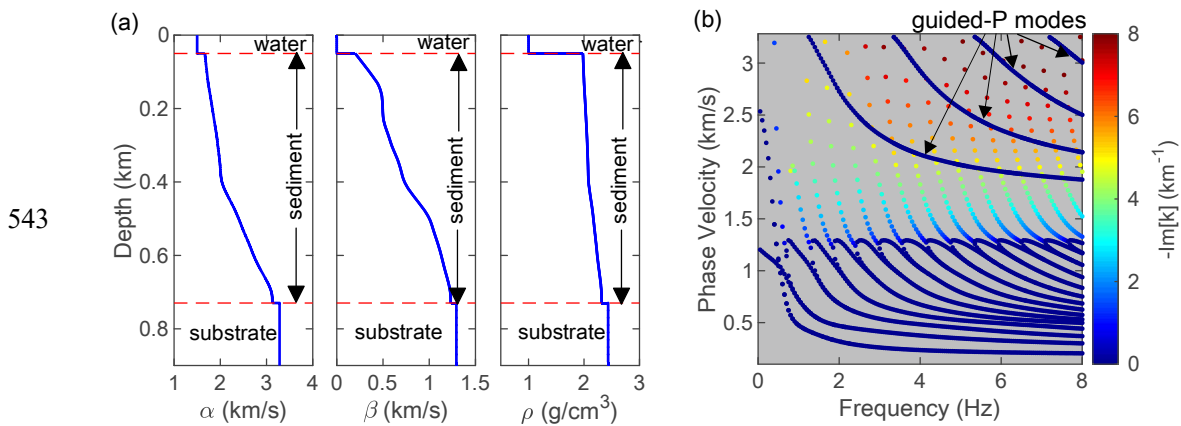
519

520 4.2 Gradient offshore model

521 Propagation-matrix-type methods assume that each layer of the multilayered 1D Earth
522 model is homogeneous. When solving for the modes accurately in a waveguide
523 composed of gradient layers, propagation-matrix-type methods become tedious unless
524 the waveguide is divided into numerous sufficiently thin layers. A significant
525 advantage of SASEM is its convenience when treating a waveguide composed of
526 gradient layers because SASEM allows the model parameters to be variable at
527 different nodes inside an element.

528 We designed a 1D inhomogeneous offshore model in which the sediment layers
 529 were covered by a 50-m-thick water layer. The density and P-wave velocity of the
 530 water layer were defined to be constant (i.e., $1 \text{ g}\cdot\text{cm}^{-3}$ and $1.5 \text{ km}\cdot\text{s}^{-1}$, respectively),
 531 whereas the parameters of the sediment layers were gradually changed (Fig. 7a). The
 532 half-space substrate was assumed to be homogeneous.

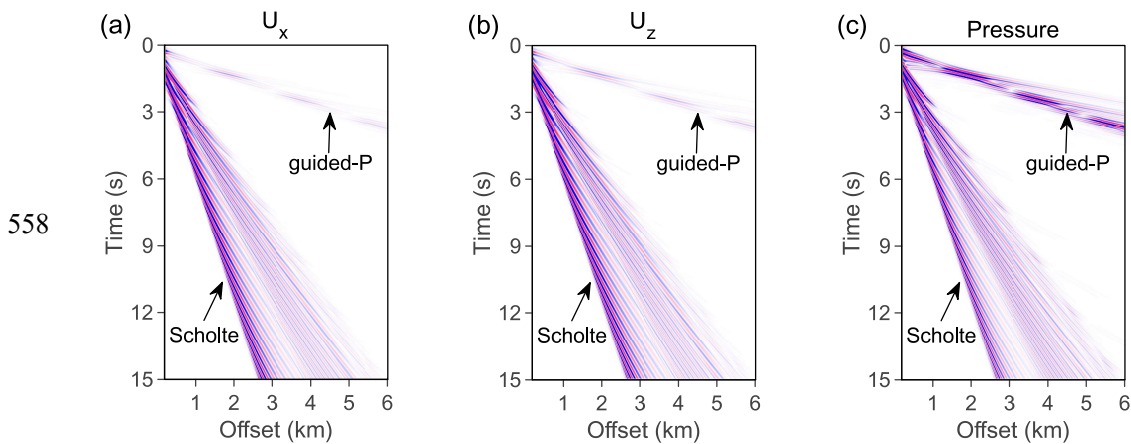
533 Similar to the treatments of the PSV wavefields in the half-space, we described
 534 the wavefields in the water layer using P-wave potentials. Following the derivation of
 535 Komatitsch et al. (2000), SASEM can handle a waveguide containing water layers
 536 with a simple modification to Eqs. (34)–(38). Appendix B provides the modified
 537 version of the eigenvalue system. Using SASEM, we calculated the normal and leaky
 538 modes of the PSV waves (Fig. 7b). In the SASEM computation, the sediment layer
 539 was divided into four sublayers with thicknesses of 0.1 km, 0.25 km, 0.15 km, and
 540 0.18 km. Then, the model discretization of each sublayer was determined using Eq.
 541 (42). Of the numerous leaky modes, several guided-P mode dispersion curves with
 542 weak attenuation can be identified in Fig. 7b.



544 Figure 7 (a) Offshore model with gradient sediment layers. (b) Modal solutions of
 545 SASEM including normal and leaky modes.

546

547 In geophysical exploration, both the guided-P modes and the normal modes of
548 offshore models are observable. As an example, we synthesized seismograms with an
549 idealized airgun source placed at a depth of 10 m and an ocean bottom node (OBN)
550 array arranged on the sea floor. The dominant frequency of the idealized airgun source
551 was 3 Hz. A total of 600 OBNs were evenly distributed on the seafloor with a
552 minimum offset of 200 m and a maximum offset of 6000 m. GRTM was used for the
553 forward modeling (Chen 1999). Because GRTM assumes that each layer of the
554 multilayered model is homogeneous, the gradient sediments were divided into 50 thin
555 layers and each thin layer was considered homogeneous. Fig. 8 shows the synthetic
556 multicomponent records in which we can find Scholte waves (controlled by normal
557 modes) and guided-P-waves (controlled by guided-P modes).



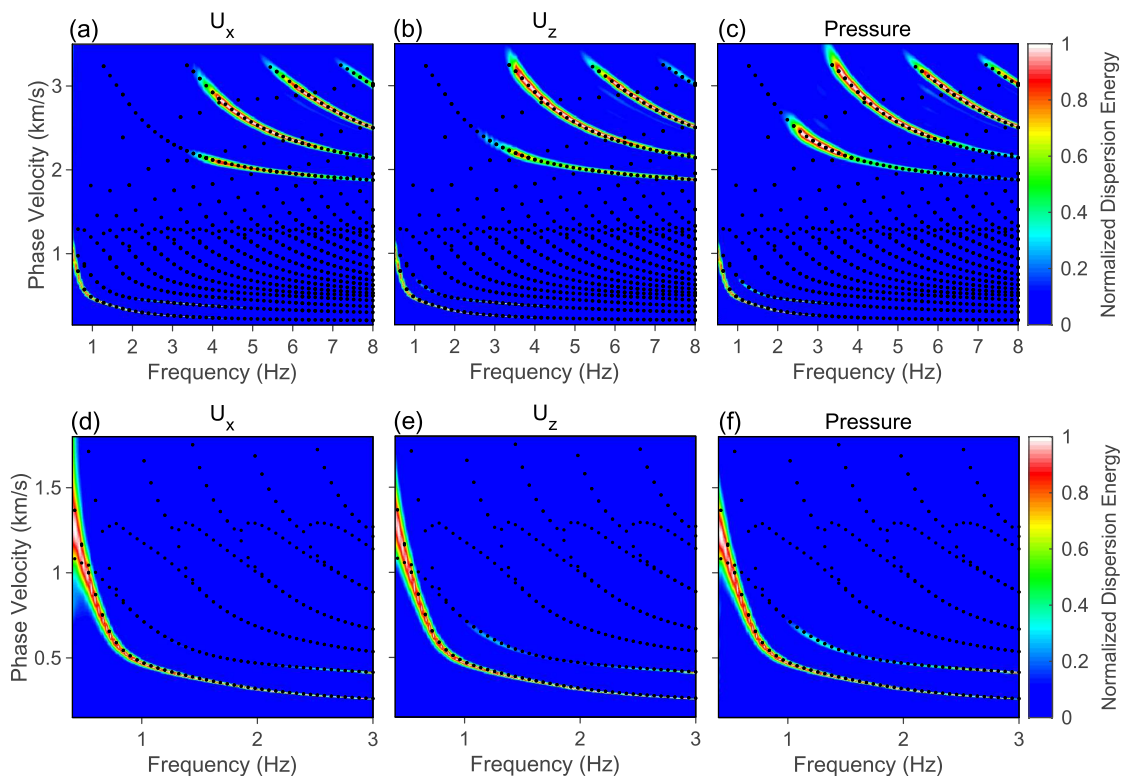
559 Figure 8 Synthetic multicomponent ocean bottom node (OBN) records

560

561 Using the frequency–Bessel transform (Forbriger 2003; Wang et al. 2019; Xi et al.
562 2021), we obtained the dispersion spectra shown in Fig. 9. In the low-phase-velocity
563 and low-frequency area of the dispersion spectra, the fundamental Scholte mode and

564 first higher normal mode can be identified. The guided-P dispersion energy occurs in
 565 the high-phase-velocity and high-frequency areas. As shown in Fig. 9, the theoretical
 566 dispersion curves calculated via SASEM perfectly match the dispersion spectra.

567 It has been reported that guided-P modes can bring more constraints to P-wave
 568 velocity structures, and several inversion tests have been conducted to retrieve P-wave
 569 velocities based on secular functions (Boiero et al. 2013) or dispersion spectra (Li et
 570 al. 2018). An inversion directly based on the dispersion curves of the guided-P modes
 571 has not yet been conducted because of the complexity of calculating leaky modes.
 572 With the proposed SASEM, the potential usage of the guided-P modes, as well as the
 573 organ-pipe modes, in dispersion inversions can be studied in the future.



574
 575 Figure 9 Dispersion spectra of the (a) horizontal, (b) vertical, and (c) pressure
 576 components. Dispersion spectra focusing on the low-frequency and low-velocity area
 577 to clearly show the Scholte modes for the (d) horizontal, (e) vertical, and (f) pressure

578 components. The black dots represent the theoretical dispersion curves as solved
579 using SASEM.

580

581 **5. CONCLUSIONS**

582 We proposed SASEM to solve for the normal and leaky modes of planar elastic
583 waveguides. Unlike root-searching methods based on secular functions, SASEM can
584 conveniently provide a high-accuracy modal solution without any prior information.
585 Additionally, no root missing occurs within the focused-on complex domains. The
586 core of SASEM consists of treatments for the transparent boundary condition in the
587 half-space substrate. The version of SASEM proposed in this paper differs from
588 former finite-element-based or spectral-element-based methods in that the modes are
589 calculated by solving a linear eigenvalue problem with the analytical transparent
590 boundary condition instead of the external and approximate boundary condition (e.g.,
591 PML and artificial viscoelastic layers).

592 Different strategies are adopted for the SH-wave modes and PSV-wave modes.
593 For the simpler SH-wave modes, the transparent boundary condition is analytically
594 combined with the displacement equation to result in a linear eigenvalue problem. For
595 the PSV-wave modes, we focus on the modes located on the $(+, +)$ and $(+, -)$
596 Riemann sheets at the present stage. The governing equations of the wavefields are
597 composed of displacement equations in the finite-thickness layers and potential
598 equations in the half-space substrate. The analytical transparent boundary condition is

599 applied to the S-wave potential wavefields. Conversely, for the P-wave potentials, a
600 semi-infinite element technique is adopted because the P-wave potentials of the
601 modes on the (+, +) and (+, -) Riemann sheets decay exponentially in the half-space.
602 After mathematical derivations, a linear eigenvalue problem is also obtained for the
603 PSV-wave modes.

604 SASEM was first validated using a multilayered crustal model, which showed
605 that the modal solutions agree perfectly with the zero points of the secular function.
606 The oscillation features of the normal and leaky modes were then analyzed, showing
607 that the leaky modes differ from the normal modes because of the increasing
608 wavefields in the half-space. An oscillation analysis of the guided-P modes confirmed
609 that the guided-P modes were primarily controlled by P-waves. A multilayered
610 gradient model was then used to demonstrate the effectiveness of SASEM when
611 applied to waveguides composed of gradient layers. The dispersion spectra extracted
612 from synthetic seismograms perfectly matched the theoretical dispersion curves.
613 These numerical tests indicate that SASEM can be an effective tool for the
614 investigation of observed leaky modes in seismograms.

615 Since the eigenvalue problem for determining the dispersion curves has been
616 theoretically derived, an inversion problem can also be constructed and solved. Based
617 on schemes similar to Haney & Tsai (2017) and Hawkins (2018), SASEM can be
618 applied to the dispersion inversion of surface waves. Moreover, SASEM provides the
619 possibility of the inversion based on leaky-mode dispersion curves, which may bring
620 more constraints on V_p structures.

621 **ACKNOWLEDGMENTS**

622 This work was supported by the Shenzhen Key Laboratory of Deep Offshore Oil
623 and Gas Exploration Technology (Grant No. ZDSYS20190902093007855), National
624 Natural Science Foundation of China (Grant No. 41790465), the leading talents of the
625 Guangdong province program (Grant No. 2016LJ06N652), and Shenzhen Science and
626 Technology Program (Grant No. KQTD20170810111725321).

627 **DATA AVAILABILITY**

628 The codes and data used in this paper will be shared upon reasonable request to
629 the corresponding author.

630 **REFERENCES**

- 631 Aki, K., & Richards, P. G., 2002. Quantitative seismology. University Science Books.
- 632 Boiero, D., Wiarda, E., & Vermeer, P., 2013. Surface-and guided-wave inversion for
633 near-surface modeling in land and shallow marine seismic data. *The Leading*
634 *Edge*, 32(6), 638-646.
- 635 Chen, C., Berini, P., Feng, D., Tanev, S., & Tzolov, V. P., 2000. Efficient and accurate
636 numerical analysis of multilayered planar optical waveguides in lossy anisotropic
637 media. *Optics Express*, 7(8), 260-272.
- 638 Chen, X., 1993. A systematic and efficient method of computing normal modes for
639 multilayered half-space. *Geophysical Journal International*, 115(2), 391-409.

640 Chen, X. F., 1999. Seismogram synthesis in multi-layered half-space Part I.
641 Theoretical formulations. *Earthquake Research in China*, 13(2), 149-174.

642 Cochran, M. D., Woeber, A. F., & De Bremaecker, J. C., 1970. Body waves as normal
643 and leaking modes, 3. Pseudo modes and partial derivatives on the (+ -) sheet.
644 *Reviews of Geophysics*, 8(2), 321-357.

645 Delves, L. M., & Lyness, J. N., 1967. A numerical method for locating the zeros of an
646 analytic function. *Mathematics of computation*, 21(100), 543-560.

647 Denolle, M. A., Dunham, E. M., & Beroza, G. C., 2012. Solving the surface - wave
648 eigenproblem with Chebyshev spectral collocation. *Bulletin of the Seismological*
649 *Society of America*, 102(3), 1214-1223.

650 Dorman, J., & Ewing, M., 1962. Numerical inversion of seismic surface wave
651 dispersion data and crust - mantle structure in the New York - Pennsylvania area.
652 *Journal of Geophysical Research*, 67(13), 5227-5241.

653 Foiret, J., Minonzio, J. G., Chappard, C., Talmant, M., & Laugier, P., 2014. Combined
654 estimation of thickness and velocities using ultrasound guided waves: A
655 pioneering study on in vitro cortical bone samples. *IEEE transactions on*
656 *ultrasonics, ferroelectrics, and frequency control*, 61(9), 1478-1488.

657 Forbriger, T., 2003. Inversion of shallow-seismic wavefields: I. Wavefield
658 transformation. *Geophysical Journal International*, 153(3), 719-734.

659 Gilbert, F., 1964. Propagation of transient leaking modes in a stratified elastic
660 waveguide. *Reviews of Geophysics*, 2(1), 123-153.

661 Glytsis, E. N., & Anemogiannis, E., 2018. Simple derivative-free method of zero

662 extraction by phase-based enclosure for determination of complex propagation
663 constants in planar multilayer waveguides. *Applied Optics*, 57(36), 10485-10494.

664 Grant, J. C., Beal, J. C., & Frenette, N. J. P., 1994. Finite element analysis of the
665 ARROW leaky optical waveguide. *IEEE journal of quantum electronics*, 30(5),
666 1250-1253.

667 Haney, M. M., & Tsai, V. C., 2017. Perturbational and nonperturbational inversion of
668 Rayleigh-wave velocities. *Geophysics*, 82(3), F15-F28.

669 Haskell, N. A., 1953. The dispersion of surface waves on multilayered media. *Bulletin*
670 *of the seismological Society of America*, 43(1), 17-34.

671 Hawkins, R., 2018. A spectral element method for surface wave dispersion and
672 adjoints. *Geophysical Journal International*, 215(1), 267-302.

673 Hayashi, T., & Inoue, D., 2014. Calculation of leaky Lamb waves with a
674 semi-analytical finite element method. *Ultrasonics*, 54(6), 1460-1469.

675 Huang, C. C., 2006. Numerical calculations of ARROW structures by pseudospectral
676 approach with Mur' s absorbing boundary conditions. *Optics express*, 14(24),
677 11631-11652.

678 Huang, W. P., Xu, C. L., Lui, W., & Yokoyama, K., 1996. The perfectly matched layer
679 boundary condition for modal analysis of optical waveguides: leaky mode
680 calculations. *IEEE Photonics Technology Letters*, 8(5), 652-654.

681 Julian, B. R., & Anderson, D. L., 1968. Travel times, apparent velocities and
682 amplitudes of body waves. *Bulletin of the Seismological Society of America*,
683 58(1), 339-366.

684 Kausel, E., 2005. Waves propagation modes: From simple systems to layered soils. In
685 Surface Waves in Geomechanics: Direct and Inverse Modelling for Soils and
686 Rocks (pp. 165-202). Springer, Vienna.

687 Knopoff, L., 1964. A matrix method for elastic wave problems. Bulletin of the
688 Seismological Society of America, 54(1), 431-438.

689 Komatitsch, D., Barnes, C., & Tromp, J., 2000. Wave propagation near a fluid-solid
690 interface: A spectral-element approach. Geophysics, 65(2), 623-631.

691 Kugler, S., Bohlen, T., Forbriger, T., Bussat, S., & Klein, G. (2007). Scholte-wave
692 tomography for shallow-water marine sediments. Geophysical Journal
693 International, 168(2), 551-570.

694 Li, J., Hanafy, S., & Schuster, G., 2018. Wave-Equation Dispersion Inversion of
695 guided-P waves in a Waveguide of Arbitrary Geometry. Journal of Geophysical
696 Research: Solid Earth, 123(9), 7760-7774.

697 Li, Z., & Chen, X., 2020. Multiple dispersion curves extracted from seismic PL phase.
698 Earth and Space Science Open Archive.

699 Lysmer, J., 1970. Lumped mass method for Rayleigh waves. Bulletin of the
700 Seismological Society of America, 60(1), 89-104.

701 Mazzotti, M., Bartoli, I., Marzani, A., & Viola, E., 2013. A coupled SAFE-2.5 D BEM
702 approach for the dispersion analysis of damped leaky guided waves in embedded
703 waveguides of arbitrary cross-section. Ultrasonics, 53(7), 1227-1241.

704 Michalski, K. A., & Mustafa, M. M., 2018. Numerically stable and reliable
705 computation of electromagnetic modes in multilayered waveguides using the

706 Cauchy integration method with automatic differentiation. IEEE Transactions on
707 Microwave Theory and Techniques, 66(9), 3981-3992.

708 Priolo, E., Carcione, J. M., & Seriani, G., 1994. Numerical simulation of interface
709 waves by high-order spectral modeling techniques. The Journal of the Acoustical
710 Society of America, 95(2), 681-693.

711 Radovich, B. J., & De Bremaecker, J. C., 1974. Body waves as normal and leaking
712 modes—leaking modes of Love waves. Bulletin of the Seismological Society of
713 America, 64(2), 301-306.

714 Robertsson, J. O. A., Holliger, K., Green, A. G., Pugin, A., & De Iaco, R., 1996.
715 Effects of near - surface waveguides on shallow high - resolution seismic
716 refraction and reflection data. Geophysical Research Letters, 23(5), 495-498.

717 Roth, M., Holliger, K., & Green, A. G., 1998. Guided waves in near - surface seismic
718 surveys. Geophysical Research Letters, 25(7), 1071-1074.

719 Roth, M., & Holliger, K., 1999. Inversion of source-generated noise in high-resolution
720 seismic data. The Leading Edge, 18(12), 1402-1406.

721 Seriani, G., Priolo, E., Carcione, J., & Padovani, E., 1992. High-order spectral
722 element method for elastic wave modeling. In Seg technical program expanded
723 abstracts 1992 (pp. 1285-1288). Society of Exploration Geophysicists.

724 Shtivelman, V., 2004. Estimating seismic velocities below the sea - bed using surface
725 waves. Near Surface Geophysics, 2(4), 241-247.

726 Smith, R. E., Houde-Walter, S. N., & Forbes, G. W., 1992. Mode determination for
727 planar waveguide using the four-sheeted dispersion relation. IEEE journal of

728 quantum electronics, 28(6), 1520-1526.

729 Strobbia, C., & Cassiani, G., 2007. Multilayer ground-penetrating radar guided waves
730 in shallow soil layers for estimating soil water content. *Geophysics*, 72(4),
731 J17-J29.

732 Sun, C., Wang, Z., Wu, D., Cai, R., & Wu, H., 2021. A unified description of surface
733 waves and guided waves with relative amplitude dispersion maps. *Geophysical
734 Journal International*, 227(3), 1480-1495.

735 Treysse, F., Nguyen, K. L., Bonnet-BenDhia, A. S., & Hazard, C., 2014. Finite
736 element computation of trapped and leaky elastic waves in open stratified
737 waveguides. *Wave Motion*, 51(7), 1093-1107.

738 Treysse, F., 2016. Spectral element computation of high-frequency leaky modes in
739 three-dimensional solid waveguides. *Journal of Computational Physics*, 314,
740 341-354.

741 Uranus, H. P., Hoekstra, H. J. W. M., & Van Groesen, E., 2004. Simple high-order
742 Galerkin finite element scheme for the investigation of both guided and leaky
743 modes in anisotropic planar waveguides. *Optical and quantum electronics*, 36(1),
744 239-257.

745 Valenciano, J., & Chaplain, M. A., 2005. A Laguerre-Legendre spectral-element
746 method for the solution of partial differential equations on infinite domains:
747 application to the diffusion of tumour angiogenesis factors. *Mathematical and
748 computer modelling*, 41(10), 1171-1192.

749 Watson, T. H. 1972. A real frequency, complex wave-number analysis of leaking

750 modes. *Bulletin of the Seismological Society of America*, 62(1), 369-384.

751 Wang, J., Wu, G., & Chen, X., 2019. Frequency-Bessel transform method for effective
752 imaging of higher - mode Rayleigh dispersion curves from ambient seismic
753 noise data. *Journal of Geophysical Research: Solid Earth*, 124(4), 3708-3723.

754 Wu, B., & Chen, X., 2016. Stable, accurate and efficient computation of normal
755 modes for horizontal stratified models. *Geophysical Journal International*, 206(2),
756 1281-1300.

757 Wu, B., & Chen, X., 2017. Accurate computation of leaky modes for anomalous
758 layered models. *Annals of Geophysics*, 60(6), S0663-S0663.

759 Wu, G. X., Pan, L., Wang, J. N., & Chen, X., 2020. S velocity inversion using
760 multimodal dispersion curves from ambient seismic noise data of USArray
761 transportable array. *Journal of Geophysical Research: Solid Earth*, 125(1),
762 e2019JB018213.

763 Xi, C., Xia, J., Mi, B., Dai, T., Liu, Y., & Ning, L., 2021. Modified frequency–Bessel
764 transform method for dispersion imaging of Rayleigh waves from ambient
765 seismic noise. *Geophysical Journal International*, 225(2), 1271-1280.

766 Xia, J., Miller, R. D., & Park, C. B., 1999. Estimation of near-surface S-wave velocity
767 by inversion of Rayleigh waves. *Geophysics*, 64(3), 691-700.

768 Zhu, J., Zhang, X., & Song, R., 2010. A unified mode solver for optical waveguides
769 based on mapped barycentric rational chebyshev differentiation matrix. *Journal*
770 *of lightwave technology*, 28(12), 1802-1810.

771

772 **APPENDIX A: GAUSS–RADAU–LAGUERRE NODES**

773 Here, we introduce the Laguerre polynomials, which can be determined using the
774 following recurrence relation:

$$\begin{aligned}
 &L_0(\xi) = 1 \\
 &L_1(\xi) = 1 - \xi \\
 &L_n(\xi) = \frac{2n-1-\xi}{n}L_{n-1}(\xi) - \frac{n-1}{n}L_{n-2}(\xi)
 \end{aligned} \tag{A1}$$

776 The Gauss–Radau–Laguerre (GRL) nodes are defined as the roots of the equation
777 $\xi L'_{n+1}(\xi) = 0$, where n denotes the order. Meanwhile, the Laguerre functions are
778 defined as

$$779 \hat{L}_n(\xi) = L_n(\xi)e^{-\xi/2}. \tag{A2}$$

780 When the function $f(\xi)$ is integrable in the range of $[0, \infty)$, the modified version
781 of the Gauss-Radau-Laguerre quadrature rule is written as (Valenciano & Chaplain,
782 2005)

$$783 \int_0^{\infty} f(\xi)d\xi \approx \sum_{j=0}^n f(\xi_j)w(\xi_j), \tag{A3}$$

784 where j denotes the index of the GRL node. The discrete weight functions are given
785 by

$$786 w(\xi_j) = \frac{1}{(n+1)\hat{L}_n(\xi_j)}. \tag{A4}$$

787 The derivatives of the Lagrangian interpolation function can be obtained via
788 (Valenciano & Chaplain, 2005)

$$789 \varphi'_i(\xi_j) = \begin{cases} \frac{\hat{L}_{n+1}(\xi_j)}{\hat{L}_{n+1}(\xi_i)(\xi_j - \xi_i)} & \text{if } i \neq j \\ 0 & \text{if } i = j \neq 0, \\ \frac{-(n+1)}{2} & \text{if } i = j = 0 \end{cases}, \tag{A5}$$

790 where i denotes the index of the Lagrangian interpolation function.

791 With the coordinates ξ , weight functions $w(\xi)$, and derivatives of the
 792 Lagrangian interpolation function $\varphi'(\xi)$, the GRL semi-infinite element can be
 793 applied in the same manner as traditional GLL finite elements.

794 APPENDIX B: SASEM FOR OFFSHORE MODELS

795 For offshore models, we assume Layer 1 to be the water layer. In the water layer,
 796 the acoustic equation is expressed as

$$797 \quad \rho_f \omega^2 p(z) - k^2 \kappa p(z) + \kappa \frac{\partial^2 p(z)}{\partial z^2} = 0, \quad (\text{B1})$$

798 where ω is the circular frequency, k is the wavenumber, p represents the P-wave
 799 potential, ρ_f represents the water density, and κ represents the bulk modulus of
 800 water. At the interface between the water and the solid materials, there is the
 801 following boundary condition:

$$802 \quad \begin{cases} U_z = -\frac{\partial p}{\partial z} \\ \tau_z = \rho_f \omega^2 p \\ \tau_r = 0 \end{cases}. \quad (\text{B2})$$

803 We assume that the first layer of the waveguide in Fig. 2 is a water layer; then, the
 804 final equation system can be obtained by modifying Eqs. (34)–(38):

$$805 \quad \int_{z_0}^{z_1} \left(\rho_f \omega^2 - \frac{\omega^2 \kappa}{\beta_{N+1}^2} \right) \bar{p}^{(1)} \phi dz + \gamma_{N+1}^2 \int_{z_0}^{z_1} \kappa \bar{p}^{(1)} \phi dz - \int_{z_0}^{z_1} \kappa \frac{\partial \bar{p}^{(1)}}{\partial z} \frac{\partial \phi}{\partial z} dz - \kappa(z) \bar{U}_z^{(2)}(z) \phi(z) \Big|_{z_1} \\ - \kappa(z) \frac{\partial \bar{p}^{(1)}(z)}{\partial z} \phi(z) \Big|_{z_0} = 0, \quad (\text{B3})$$

$$\begin{aligned}
& \int_{z_1}^{z_N} \left(\rho\omega^2 - \frac{\omega^2(\lambda+2\mu)}{\beta_{N+1}^2} \right) U_r \varphi dz + \gamma_{N+1}^2 \int_{z_1}^{z_N} (\lambda+2\mu) U_r \varphi dz - \int_{z_1}^{z_N} \left(\lambda \frac{\partial \bar{U}_z}{\partial z} \varphi - \mu \bar{U}_z \frac{\partial \varphi}{\partial z} \right) dz \\
& - \int_{z_1}^{z_N} \mu \frac{\partial U_r}{\partial z} \frac{\partial \varphi}{\partial z} dz + \left[2\mu_{N+1} \frac{\partial \bar{p}^{(N+1)}(z)}{\partial z} - 2\gamma_{N+1}^2 \mu_{N+1} q^{(N+1)}(z) + \frac{\omega^2 \mu_{N+1}}{\beta_{N+1}^2} q^{(N+1)}(z) \right] \varphi(z) \Big|_{z=z_N} = 0,
\end{aligned} \tag{B4}$$

$$\begin{aligned}
& \int_{z_1}^{z_N} \left(\rho\omega^2 - \frac{\omega^2 \mu}{\beta_{N+1}^2} \right) \bar{U}_z \varphi dz + \gamma_{N+1}^2 \int_{z_1}^{z_N} \left(\mu \bar{U}_z \varphi - \mu \frac{\partial U_r}{\partial z} \varphi + \lambda U_r \frac{\partial \varphi}{\partial z} \right) dz \\
& + \frac{\omega^2}{\beta_{N+1}^2} \int_{z_1}^{z_N} \left(\mu \frac{\partial U_r}{\partial z} \varphi - \lambda U_r \frac{\partial \varphi}{\partial z} \right) dz - \int_{z_1}^{z_N} (\lambda+2\mu) \frac{\partial \bar{U}_z}{\partial z} \frac{\partial \varphi}{\partial z} dz - \rho_f \omega^2 p^{(1)}(z) \varphi(z) \Big|_{z_1} \\
& + \left[\left(\frac{\omega^2}{\beta_{N+1}^2} - \gamma_{N+1}^2 \right) \lambda_{N+1} \bar{p}(z) - (\lambda_{N+1} + 2\mu_{N+1}) \frac{\partial^2 \bar{p}(z)}{\partial z^2} \right] \varphi(z) \Big|_{z=z_N} = 0 \\
& + 2i\omega^2 \rho_{N+1} \gamma_{N+1} q(z) - 2i\mu_{N+1} \gamma_{N+1}^3 q(z)
\end{aligned} \tag{B5}$$

$$\int_{z_N}^{z_\infty} \left(\rho\omega^2 - \frac{\omega^2(\lambda+2\mu)}{\beta_{N+1}^2} \right) \bar{p}^{(N)} \varphi dz + \gamma_{N+1}^2 \int_{z_N}^{z_\infty} (\lambda+2\mu) \bar{p}^{(N)} \varphi dz - \int_{z_N}^{z_\infty} (\lambda+2\mu) \frac{\partial \bar{p}^{(N)}}{\partial z} \frac{\partial \varphi}{\partial z} dz = 0, \tag{B6}$$

$$\rho_{N+1} \omega^2 \bar{p}^{(N+1)}(z_N) = (\lambda_N + 2\mu_N) \frac{\partial \bar{U}_z^{(N)}(z)}{\partial z} \Big|_{z=z_N} + (\lambda_N + 2\mu_{N+1}) \left(\frac{\omega^2}{\beta_{N+1}^2} - \gamma_{N+1}^2 \right) U_r^{(N)}(z_N), \tag{B7}$$

$$\rho_{N+1} \omega^2 q^{(N+1)}(z_N) = - \left[\mu_N \frac{\partial U_r^{(N)}(z)}{\partial z} \Big|_{z=z_N} - \mu_N \bar{U}_z^{(N)}(z_N) \right] - 2\mu_{N+1} \bar{U}_z^{(N)}(z_N), \tag{B8}$$

812 where Eq. (B3) determines the P-wave potentials in the water layer. The discretization
813 of Eqs. (B3)–(B8) using SASEM leads to an eigenvalue problem similar to Eq. (39).